Chemical Physics 144 (1990) 249–263
North-Holland

EXCITATION OF HgI(B), CdI(B), ZnI(B), PbI(B), CdBr(B), AND ZnBr(B) BY EXCITATION-TRANSFER REACTIONS OF N_2(A) WITH THE DIHALIDE COMPOUNDS

N. SADEGHI, J.C. PEBAY-PEYROULA
Laboratoire de Spectrométrie Physique, Université Joseph Fourier–Grenoble 1, B.P. 87, 38402 St. Martin d'Heres Cedex, France

D.W. SETSER and Glenn LO
Department of Chemistry, Kansas State University, Manhattan, KS 66506, USA

Received 9 March 1990

The reactions of $N_2(A\,^3\Sigma_u^+)$ with HgI_2, CdI_2, ZnI_2, PbI_2, $CdBr_2$, and $ZnBr_2$ have been investigated in a flowing afterglow reactor at 300 K. The total quenching rate constants are in the range of 5×10^{-10} cm^3 s^{-1}. The HgI_2 and CdI_2 reactions gave moderately strong HgI(B–X) and CdI(B–X) emission with branching fractions for HgI(B) and CdI(B) formation of 0.1–0.2. The branching fraction for ZnI(B) formation from ZnI_2 was much less than from CdI_2 and the emission from the PbI_2, $CdBr_2$ and $ZnBr_2$ reactions was insignificant. The trend of reduced branching ratio for the lighter dihalides of Cd resembles the results found for N_2(A) with mercury dihalides. The HgI(B–X) spectrum from $N_2(A)+HgI_2$ was fitted with a truncated Boltzmann vibrational distribution corresponding to $\langle f_v\rangle=0.44$. The CdI(B) and CdI(X) potentials were developed in order to simulate the CdI(B–X) spectrum. A truncated Boltzmann vibrational distribution of CdI(B, v') levels with $\langle f_v\rangle=0.28$ was inferred. A revision for ω_e' of ZnI(B) is suggested.

1. Introduction

Dissociative reactions of group IIb metal dihalides, MX_2, are of interest because electronically excited states of the monohalides can be formed, and these are useful visible light sources [1–7]. Furthermore, the systems are sufficiently simple to be of interest for comparison with theoretical models [6–12]. In this work we have studied the dissociative excitation-transfer reactions of HgI_2, PbI_2, CdX_2 and ZnX_2 (X=Br and I) with $N_2(A\,^3\Sigma_u^+)$ in a flow reactor:

$$N_2(A)+MX_2$$
$$\rightarrow MX(B)+X(^2P_{3/2}\text{ or }^2P_{1/2})+N_2(X)\,, \quad (1a)$$
$$\rightarrow M+2X(^2P_{1/2}\text{ or }^2P_{3/2})+N_2(X)\,, \quad (1b)$$
$$\rightarrow MX(X)+X(^2P_{1/2}\text{ or }^2P_{3/2})+N_2(X)\,. \quad (1c)$$

The $N_2(A, v'=0$ and 1) molecules can provide 6.17 and 6.35 eV of energy, but the more favorable Franck–Condon pathways for $N_2(X, v'')$ formation correspond to ≈ 5 eV. The total quenching rate constant, k_Q, corresponds to the sum of the rate constants for the three possible channels in (1). The branching fractions for MX(B) formation, $\Gamma_{MX(B)}$, are of primary interest. The first excited state, MX(A), is dissociative and this exit channel is the same as (1b). Although the spectroscopy of the B–X transitions of CdI and ZnI are not well established, both systems have been shown to be laser systems under photodissociative (193 nm) and discharge excitation of CdI_2 and ZnI_2 [4,13,14]. The HgX(B–X) transitions are established laser systems [15,16].

Fig. 1 shows a general correlation diagram, based on calculations for $HgBr_2$ [9], that illustrates the expected dissociation pattern for the MX_2^* states that lie within the energy range of N_2(A). Photolysis in the second absorption band giving $HgX_2(1\,^1\Sigma_u^+)$ can lead to relatively high quantum yields for HgX(B) [1]. Fluorescence polarization measurements from HgBr(B–X) show that $HgBr_2(1\,^1\Sigma_u^+)$ is indeed the precursor state, even though the stable geometry of the excited state is bent [10,11]. The $HgX_2(1\,^1\Sigma_u^+)$ state moves to higher energy in the X=I, Br, Cl se-

0301-0104/90/$ 03.50

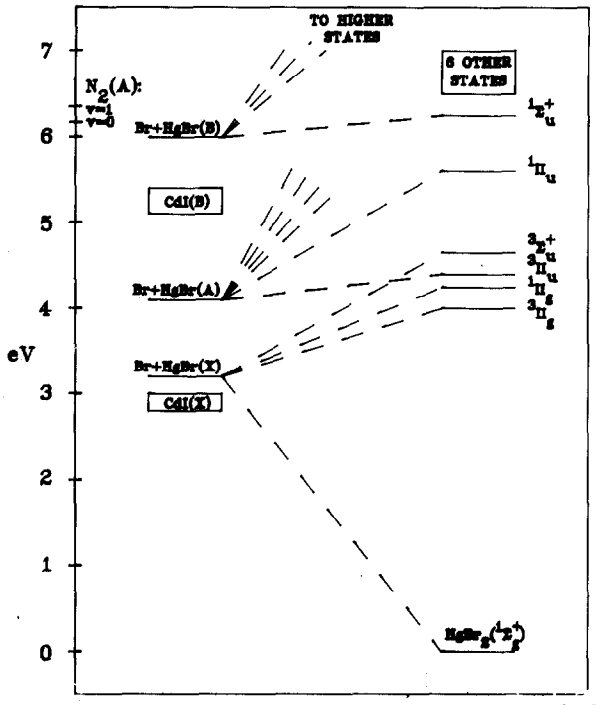

Fig. 1. Dissociation pathways for MX_2 according to the calculated results [9] for $HgBr_2$. The 6 low excited states arise from promotion of an electron from the $2\pi_g$, $1\pi_u$ or $2\sigma_u$ orbitals to the $4\sigma_g$ empty orbital, which is essentially the Hg(6s) orbital. The next 6 excited states correspond to promotion of an electron from the $2\pi_g$ to the $2\pi_u$ orbital; these states presumably are above the energy provided by $N_2(A)$. The calculated energies of the $^1\Pi_u$ and $^1\Sigma_u^+$ states have been increased to match the positions of the $HgBr_2$ absorption bands. The positions of the CdI(X and B) states have been added for reference.

ries. If the $N_2(A)$ excitation-transfer reaction gives the triplet states lying immediately above the $HgX_2(1\,^1\Sigma_u^+)$ state, dissociation to HgX(B) can occur via intersystem crossing to the $\tilde{A}\,^1\Sigma_u^+$ state. The lower energy triplet states do not directly correlate to HgX(B). If the triplet state energies resemble those for the singlet states, the increase in energy for X=Cl explains why $\Gamma_{HgCl(B)}$ was negligible for $HgCl_2$ and CH_3HgCl reacting with $N_2(A)$, whereas $\Gamma_{HgBr(B)}$ was ≈ 0.2 for the corresponding bromine compounds [7,8]. The absorption spectrum of CdI_2 resembles that for $HgBr_2$ [1], which implies that the excited states of CdI_2 should have an energy pattern resembling those shown in fig. 1. In the work to be presented, we found that the $\Gamma_{MX(B)}$ were about 0.15 for HgI_2 and CdI_2, approximately 0.01 for ZnI_2, and negligible for $CdBr_2$ and $ZnBr_2$. This is consistent with the expectation that the $\tilde{A}\,^1\Sigma_u^+$ and nearby triplet states of $CdBr_2$ and $ZnBr_2$ are higher in energy than for ZnI_2 and CdI_2. Fig. 1 is an oversimplification, since the stable geometry for the first six $HgBr_2$ excited states are bent and spin–orbit effects have not been included. One demonstration of the actual complexity is that photolysis of HgI_2 or CdI_2 in the first absorption band ($^1\Pi_u$ state) gives significant amounts of HgI(X) or CdI(X) + I($^2P_{3/2}$ and $^2P_{1/2}$) rather than the predicted (1b) channel [11,12]. Since the PbI(A, B) yield was negligible, the excited states of PbI_2, which do not fit the scheme of fig. 1, will not be discussed.

The CdX_2 and ZnX_2 compounds have lower vapor pressure than the HgX_2 compounds and vaporization from a heated crucible inside a flow reactor is necessary to study reaction (1), whereas the $HgBr_2$ and $HgCl_2$ vapor could be entrained in a flow of Ar that was passed through a heated glass reservoir [7]. Since a calibrated flow reactor for study of high-temperature reagents was in operation in the Grenoble Laboratory [17,18], experiments were done to record the spectra from HgI_2, CdI_2 and ZnI_2 and to measure the branching fractions. The emissions from the $ZnBr_2$, $CdBr_2$ and PbI_2 reactions, unfortunately, were too weak to study. Furthermore, $CdBr_2$ and $ZnBr_2$ were found to be so hygroscopic that the total quenching rate constant measurements were not reproducible. The experiments with HgI_2 complete the HgX_2 series [7,8] and also provide a reference for CdI_2 and ZnI_2.

The HgI(B–X) spectrum was simulated using established HgI(B and X) potentials to assign the HgI(B) vibrational distribution. Combining known information about the CdI(B and X) states with interpretations from our spectra, we were able to improve the CdI(B and X) potentials. The ZnI(B–X) spectrum also was used to discuss the ZnI(B and X) potentials. After obtaining the improved potentials, a spectral simulation was done to establish the CdI(B) vibrational distribution. Based upon the HgI(B) and CdI(B) vibrational distributions and the $\Gamma_{MI(B)}$ values, the dissociation dynamics for the HgI_2^* and CdI_2^* states formed by reaction (1a) seem to resemble the previously discussed $HgBr_2^*$ case [2,8].

Table 1
Summary of thermochemistry (eV)

Compound	D_1+D_2	D(MX–X)	D(M–X)	T_e(MX(B))
HgI_2	2.96 [a]	2.60 [a]	0.36 [a,b]	2.98 [b]
CdI_2	4.04 [a]	2.49 [c]	1.55 [c], 1.40 [d]	2.86 [e]
$CdBr_2$	5.30 [a]	3.0 [e]	2.3 [f]	
ZnI_2	4.47 [a]	$\leqslant$3.1 [g], 2.4 [h]	$\approx$2.0 [h]	$\approx$3.1
$ZnBr_2$	5.81 [a]			
PbI_2	4.34 [i]	2.35 [i]	2.00 [i]	2.5 [j]

[a] From ΔH_f^0 data for MX_2, M and X [19–22]. [b] From ref. [26].
[c] From ref. [24], which is consistent with translational energy measurements in ref. [11].
[d] From the Morse relationship $D_e=\omega_e/4\omega_e x_e$ using ω_e and $\omega_e x_e$ derived from vibrational structures of the C–X, D–X and E–X bands of CdI, see text for the values.
[e] This work, see table 2.
[f] Vendeneyev et al. suggest that $D_1\approx D_2$, but the trend for the other molecules suggests $D_1>D_2$ and these values were estimated by comparison to the trend for CdI_2.
[g] Assigned from the λ_{min} from our spectrum. [h] From ref. [3].
[i] From ref. [25]. [j] From ref. [22], for the PbI(A–X) transition.

The thermochemistry [19–26], see table 1, for the CdX_2 and ZnX_2 compounds is not well documented, although the sum of the dissociation energies should be reliable since the $\Delta H_f^0(MX_2)$ values are known [19–21]. The product translational energy measurements [11] from photolysis (300 nm) of CdI_2 seem to agree with the D(I–CdI) from the older thermochemical data [23], and the individual bond energies are known best for HgI_2 [21,26], CdI_2 [11,23], and PbI_2 [25]. There may be large uncertainties in the individual bond energies for ZnI_2, $CdBr_2$, and $ZnBr_2$. According to the estimates in table 1, the D(X–MX) values are comparable to those for HgX_2: however, the D(X–M) values are larger than for the analogous HgX molecules. The sum of D(MX–X) and T_e, which is the minimum energy required for reaction (1), is larger than 5 eV, except for PbI_2. Thus, nearly all of the available energy is required to generate MX(B) molecules by reaction (1a).

2. Experimental techniques

The experiments were done in a flowing afterglow reactor in which the MX_2 salts (Ventron or Prolabo) were vaporized from a small heated alumina crucible located inside the flow reactor. The temperature in the reaction zone was close to 300 K, since the Ar flow was not pre-heated. The apparatus, which utilized a weak dc discharge to produce metastable Ar atoms, has been described in detail [17]. The reaction of Ar($^3P_{0,2}$) atoms with N_2 was used to generate N_2(A) in the absence of N atoms [27]. The $N_2(C\,^3\Pi_u)$ molecules produced by the excitation-transfer reaction with Ar($^3P_{0,2}$) give $N_2(B\,^3\Pi_2)$ by radiative cascade and, finally, N_2(A) in a second radiative step. The N_2 flow was added to the Ar flow immediately after the discharge. Typical operating conditions were $\approx$1 Torr with $\approx$20% N_2 for a flow velocity of 20 m s^{-1}. Although the N_2(A–X) emission was not directly observed in this work, the N_2(A, $v'=1$) concentration for these operating conditions contributes about 30% to the total N_2(A) concentration and the N_2(A, $v'\geqslant 2$) concentration is negligible [28]. The MX_2 flow rates were determined from the weight loss from the crucible for a given time period of operation. The MX_2 concentration then were determined from the flow rate of the salt, the total Ar+N_2 flow rate and the total pressure. Difficulties were encountered for the MBr_2 compounds because their hygroscopic nature prevented accurate weight measurements under atmospheric conditions. Reliable spectra for known [MX_2] were obtained only with HgI_2, CdI_2 and ZnI_2.

The spectral region of principal interest was from 350 to 800 nm for the HgI(B), CdX(B) and ZnX(B) emissions. However, it also was necessary to observe the NO(A–X) emission in the 210–300 nm region for monitoring the [N_2(A)] and for comparison to the MI(B–X) intensities. A 1 m monochromator

(HR 1000 J–Y) fitted with a holographic grating and a Hamamatsu (R-955) photomultiplier tube was used to compare the visible and ultraviolet emission intensities. The wavelength response of the detection system was calibrated with standard deuterium and tungsten filament lamps, as well as branching ratios from atomic lines and molecular bands [18]. The HgI(B–X), CdI(B–X) and ZnI(B–X) spectra presented in figs. 2–4 were recorded with a 0.25 m Jarrel–Ash monochromator with gratings blazed at 300 and 600 nm and equipped with a 700-pixel intensified diode-array multichannel detector (Spectroscopy Instruments). The spectral resolution of the system was around 0.4 nm. These spectra were obtained at low Ar pressure, ≈ 0.2 Torr, in order to avoid vibrational relaxation. The higher-resolution HgI(B–X) spectrum was obtained with the 1 m monochromator and the diode-array detector (spectral resolution of 0.1 nm).

The total quenching rate constants, as well as the MI(B) product formation rate constants, were measured by reference to the reaction with NO, which has unit branching fractions for NO(A) formation,

$$N_2(A)+NO \rightarrow N_2(X)+NO(A\,^2\Sigma^+)\,. \qquad (2)$$

The rate constant for this reaction has been carefully measured and a value of $0.66 \pm 0.10 \times 10^{10}$ cm^3 molecule s^{-1} has been recommended with no significant difference for either $N_2(A, v'=0$ or 1) [29]. The

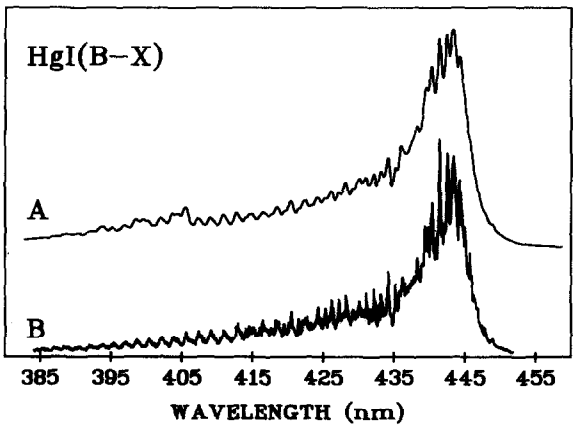

Fig. 2. Emission spectra of HgI(B–X) from $N_2(A)+HgI_2$ at 0.2 Torr. (a) Low-resolution spectrum, (b) higher-resolution spectrum. The spectra have been corrected for wavelength response of the detection system.

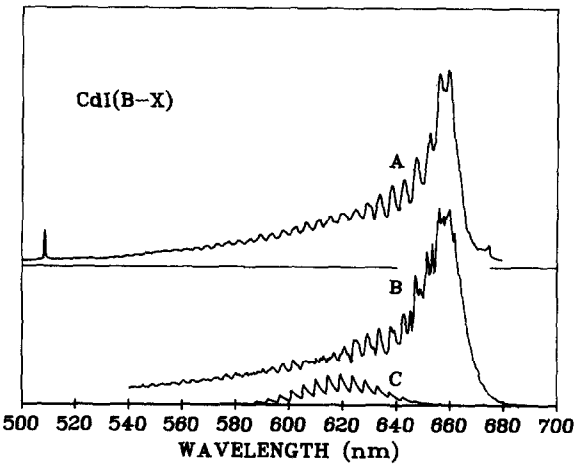

Fig. 3. Emission spectrum, plot (A), of CdI(B–X) from $N_2(A)+CdI_2$ at 0.2 Torr pressure. The spectrum has been corrected for wavelength response of the detection system. A Cd line is observed at 5085.8 Å. The simulated spectrum for a truncated 3000 K vibrational distributions is shown in plot (C), see text for further details about the calculation. The 0–v'' bands are indicated in the bottom panel, plot (C). The favored transitions from $v'=0$ are to the $v''=43$ and 44 levels.

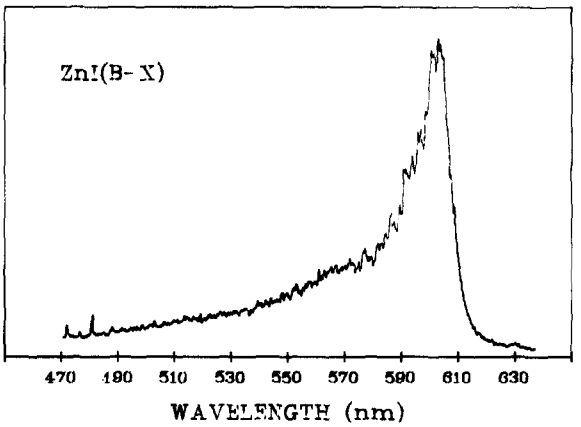

Fig. 4. Emission spectrum of ZnI(B–X) from $N_2(A)+ZnI_2$ at 0.2 Torr. The spectrum has been corrected for wavelength response of the detection system. Two Zn lines are observed at 4810.5 and 4722.2 Å.

product formation rate constants from (1a) were obtained by comparing the MI(B–X) intensity to the NO(A–X) intensity from reaction (2) for the first-order concentration regime with the same $[N_2(A)]$ and known [NO] and $[MI_2]$,

$$k_{MI(B)} = k_{NO(A)} \frac{[NO]}{[MI_2]} \frac{I_{MI(B)}}{I_{NO(A)}} . \quad (3)$$

In fact, the MI(B–X) and NO(A–X) intensities were recorded by simultaneously flowing NO and MI_2, since the two emission spectra do not interfere. The intensity terms in eq. (3) are integrated intensities that were corrected for wavelength response. The lifetimes for both NO(A) and MX(B) are very short and no consideration need be given for quenching. One experimental difficulty was the loss of transmission through the windows to the NO(A–X) emission because of a slight deposition of a MX_2 film. This film could be removed from the windows by cleaning with water.

The total quenching rate constants for MI_2 was measured by monitoring the decay of $N_2(A)$ versus distance for a known $[MI_2]$ flow rate. A small NO flow, d_1, was added to serve as tracer of $[N_2(A)]$ and the monochromator was moved along the flow reactor to monitor the decay rate of $N_2(A)$. The distance for the decay measurements was 8 cm. The slope of the $\log[N_2(A)]$ versus distance (or time) plot is the sum of $k_{MI_2}[MI_2] + k_{NO}[NO]_{d_1}$. In order to avoid the need to calibrate the conversion of distance to time, the same experiment was done without MI_2 and with enough NO added, i.e. $[NO]_{d_2}$ to obtain the same decay plot. The flow rates of NO and MI_2 can be used to obtain k_{MI_2}, since k_{NO} is known. Visual inspection of the mixing for NO and MX_2, which were added to the flow via approximately point sources, showed that the mixing for MI_2 was slow because of the smaller diffusion coefficient. Therefore, a factor of 1.3 was included to approximately correct for the slower mixing by MX_2 relative to NO.

3. Experimental results

3.1. Reactions with HgI_2, CdI_2 and ZnI_2

Evaporation of HgI_2, CdI_2 or ZnI_2 into the $N_2(A)$ flow gave a blue flame from HgI(B–X) and red flames from the CdI(B–X) and ZnI(B–X) transitions. Representative spectra are shown in figs. 2–4. The maxima in the spectra near 445, 660 and 605 nm identify the HgI(B–X), CdI(B–X), and ZnI(B–X) transition, respectively [26,3,4]. If the N_2 flow was stopped, the blue or red emissions disappeared and were replaced by the Cd and Zn atomic emission from reaction with $Ar(^3P_{0,2})$ atoms [17,19]. The appearance of the spectra in figs. 2–4 is rather typical of the spectra associated with low vibrational levels of MX(B) [2,6–8], and they resemble the HgBr(B–X) spectra from photolysis (193 nm) or from the $N_2(A)$ excitation-transfer reaction with $HgBr_2$. The regular, but rather extended, structured features in figs. 2–4 result from overlapping vibrational bands from several low v' levels (including transition from the different isotopic molecules) to a common range of high v'' levels. Higher-resolution spectra reveal finer features of the HgI spectrum (see fig. 2), but the higher-resolution CdI and ZnI emission spectra were identical with the spectra shown in figs. 3 and 4. The HgI(B–X) spectrum of fig. 2 will be simulated in section 4 to obtain the HgI(B) vibrational distribution. After improving the potentials for CdI(X) and CdI(B), the vibrational distribution of CdI(B) also was estimated from simulation of the CdI(B–X) spectrum in fig. 3. The ZnI(B) and ZnI(X) potentials are discussed, but the ZnI(B–X) spectrum was not simulated.

The absence of $Cd(^3P_1)$ and $Hg(^3P_1)$ emission from the $N_2(A) + CdI_2$, ZnI_2 and HgI_2 systems is significant. Excitation transfers from $N_2(A)$ to Cd and Hg (and probably Zn) are fast reactions [28], and the absence of these emissions imply that reaction (1b) is not very important for CdI_2, ZnI_2 and HgI_2.

The rate constant for MI(B) formation was measured for M=Cd, Hg and Zn by comparison to the NO(A) formation in reaction (2). Two independent comparisons of the relative intensities gave $k_{CdI(B)} = (0.78 \pm 0.20) k_{NO}$, or $(0.52 \pm 0.15) \times 10^{-10}$ cm^3 s^{-1}; $k_{HgI(Br)} = (2.0 \pm 0.2) k_{NO}$ or $(1.3 \pm 0.3) \times 10^{-10}$ cm^3 s^{-1} and $k_{ZnI(B)} = (0.08 \pm 0.03) k_{NO}$ or $(0.053 \pm 0.02) \times 10^{-10}$ cm^3 s^{-1}. The MI_2 total quenching rate constants also were measured relative to k_{NO} as described in section 2. The results of three independent determinations gave $k_{CdI_2} = (7.6 \pm 2) k_{NO}$ or $(5.0 \pm 1.5) \times 10^{-10}$ cm^3 $molecule^{-1}$ s^{-1}; therefore $\Gamma_{CdI(B)}$ is 0.10. These experiments with HgI_2 gave $k_{HgI_2} = (15 \pm 3) k_{NO}$ or $(10 \pm 2.5) \times 10^{-10}$ cm^3 s^{-1}; therefore $\Gamma_{HgI(B)} = 0.13$. Experiments with ZnI_2 gave $k_{ZnI_2} = (7.6 \pm 2) k_{NO}$ or $(5.0 \pm 1.5) \times 10^{-10}$ cm^3 s^{-1}, giving $\Gamma_{ZnI(B)} = 0.01$.

3.2. Reactions with $CdBr_2$, $ZnBr_2$ and PbI_2

Evaporation of $CdBr_2$ or $ZnBr_2$ into the $N_2(A)$ flow gave very weak emissions in the 500–830 nm region. The intensities were more than one order of magnitude smaller than from ZnI_2. The weak nature of the emission plus the declining response of the optical detection system prevented us from obtaining useful spectra, although the emissions surely are the CdBr(B–X) and the ZnBr(B–X) transitions [30]. Since the fluorescence was weak, no attempt was made to measure product formation rate constants. One feature of interest from $CdBr_2$ was the observation of the $Cd(^3P_1)$ resonance line at 326.1 nm. This probably arises from the secondary reaction between the Cd formed by (1b) and $N_2(A)$. This implies that channel (1b) is more important for $CdBr_2$ than for CdI_2. Quenching rate constant measurements were attempted for $CdBr_2$ and $ZnBr_2$, but accurate weight loss measurements from the crucible were not possible because of the hygroscopic nature of the materials. However, quenching of $N_2(A)$ readily occurred upon vaporization of $CdBr_2$ and $ZnBr_2$ and the quenching rate constant must be in the range of 2–5×10^{-10} cm^3 s^{-1}. The quenching rate constant for PbI_2 was measured and $k_{PbI_2}=(2.7\pm1)k_{NO}$ or $(1.8\pm0.7)\times10^{-10}$ cm^3 s^{-1}. Emission from PbI(A–X) at $\approx$487 nm could not be observed.

4. Discussion

4.1. Interactions of $N_2(A)$ and MX_2: Γ_{MX} values

Previous studies of $HgCl_2$ and $HgBr_2$ [5–8] and the present work provide an overview of the $N_2(A)+MX_2$ reactions. Due to the difficulty of reliably measuring the MX_2 flows, the uncertainties in the k_Q values are possibly as large as $\pm$50%. The rate constant for $HgCl_2$ was the smallest, 0.3×10^{-10} cm^3 s^{-1}, and that for HgI_2 was the largest, 10×10^{-10} cm^3 s^{-1}. The other values tend to be between 1.5 and 5.0×10^{-10} cm^3 s^{-1}. The total 300 K rate constants evidently are large, $1\text{–}10\times10^{-10}$ cm^3 s^{-1}, as would be expected for metallic compounds containing halogens. The rate constants for HgX_2 increase with the atomic number of the halogen. This trend, which also has been found for quenching of $N_2(A)$ by other homologous series [31,32], correlates with the increasing number of accessible acceptor states in the reagent. The lower-energy MX_2 triplet states shown in fig. 1 probably are the favored acceptor states. Since these triplet states do not correlate to MX(B), the branching fraction for $\Gamma_{MX(B)}$ is not large.

In our previous study, $k_{NO}=10\times10^{-11}$ cm^3 s^{-1} was used [7] for the reference reaction. Thus, the branching ratios reported in that work need to be reduced by a factor of 0.66 for comparison with the values here and $\Gamma_{HgBr(B)}$ becomes 0.11, which is very similar to the branching ratios from HgI_2 and CdI_2. Chang and Burnham [5] reported a rather large $k_{HgBr(B)}$ value of 1×10^{-10} cm^3 s^{-1}. However, they used the $Xe(^3P_2)+NF_3$ reaction as a reference reaction rather than reaction (2). Recent work [33] has resulted in a reduction of Γ_{XeF^*} from $Xr(^3P_2)+NF_3$ by a factor of $\approx$4 and the former discrepancy in $\Gamma_{HgBr(B)}$ from $HgBr_2$ [5,7] is now largely resolved in favor of the lower value. We conclude that the $\Gamma_{MX(B)}$ values for HgI_2, CdI_2 and $HgBr_2$ are between 0.10 and 0.15 and the $N_2(A, v'=0, 1)$ reactions at 300 K do not efficiently generate MX(B). The efficiency is even less for ZnI_2, $ZnBr_2$, $CdBr_2$ and PbI_2. The $\langle f_V(MX(B))\rangle$ values for HgI and CdI, which are presented in section 4.2, are in the 0.25–0.45 range. These are similar to the average vibrational energy reported for HgBr(B). Thus, the dissociation dynamics are evidently quite similar. These average values are based upon the total available energy from $N_2(A, v'=0)$. Since the HgX_2^* or CdI_2^* molecules may not acquire all of the energy, the dissociation of MX_2^* efficiently converts excess energy into vibrational energy of MX(B). The simulations for HgI(B–X) given in section 4.2 suggest that the rotational distribution is not highly excited. Due to the uncertain amount of energy transferred to the MX_2^* molecules, we made no effort to infer limits to bond energy from the short wavelength limits of the spectra.

The MX_2^* states that lead to MX(B) probably are the triplet states shown as being above the $^1\Sigma_u^+$ state on fig. 1. The stable geometries are bent and the bending vibration may facilitate interaction with the $^1\Sigma_u^+$ state, followed by dissociation to MX(B). Other possibilities for MX(B) formation are direct excitation to $^1\Sigma_u^+$ or formation of high vibrational states of the lower triplet states. The low $\Gamma_{MX(B)}$ values appear to be a consequence of the energy constraint pro-

vided by the $N_2(A)$ molecule. The best cases are the MI_2 molecules, which have the lowest-energy excited states and probably the largest coupling factors between the triplet MI_2^* states and the $1\,^1\Sigma_u^+$ potential, which correlates to MI(B).

The excitation-transfer reactions of $HgCl_2$ and $HgBr_2$ with $Xe(^3P_2, 8.3\ eV)$ are very efficient sources of HgX(B) molecules with $\Gamma_{HgX(B)} \approx 0.9$. The $\langle f_V(HgX) \rangle$ is ≈ 0.4 [34], which is slightly higher than for the $N_2(A)$ reactions. The reaction of $Xe(^3P_2)$ with HgI_2 has not been studied, but by analogy to $HgBr_2$, efficient HgI(B) formation would be expected. On the other hand, the reaction between $Xe(^3P_2)$ and CdI_2 results in complete dissociation with formation of Cd* [17]. The $Xe(^3P_2)+HgX_2$ reactions have been discussed in terms of a charge transfer intermediate, $Xe^+; HgX_2^-$, which evolves to HgX(B). A different mechanism apparently exists for the interaction between $Xe(^3P_2)$ and CdI_2. The $Kr(^3P_2, 10.5\ eV)$ reaction with $HgCl_2$ and $HgBr_2$ gave both HgX(B) and $Hg(^3P_1)$ emission. A comprehensive study of these MX_2 systems with various excited states of Xe would be worthwhile.

4.2. Simulation of HgI(B–X) spectra from $HgI_2+N_2(A)$

The envelope of the $HgI(B\,^2\Sigma^+ \rightarrow X\,^2\Sigma^+)$ spectrum from the reaction of HgI_2 with $N_2(A)$ resembles that from $Hg(^3P_2)+I_2$, see fig. 9 of ref. [26]. However, the spectrum in fig. 2 has a narrow oscillatory structure that is superimposed on the broad envelope. In both cases, the spectrum may be associated with the nascent vibrational distribution because the lifetimes of the HgI(B, v') levels are in the 20–100 ns [26] range and the spectra were acquired at 0.2 Torr.

Simulation of the HgI(B–X) spectrum was straightforward because the potentials and the transition dipole moment function are known [26]. The low-energy portions of these potentials are based on an analysis of the bound–bound emission bands from low v' levels [35]. Morse-type extensions were used to extend the potentials to higher energies for small internuclear distances. A Morse-type extension also was used for HgI(X) at higher energy and larger distance, but a truncated Rittner extension was used at larger distance for the HgI(B) state. The rotational constants are based on the ab initio R_e values. These potentials were satisfactory for fitting the HgI(B–X) emission spectra from reactions of $Hg(^3P_2)$ with several RI molecules [26]. Fig. 5 shows the calculated emission from selected v' levels for the potential corresponding to $J=0$. The band origins for $v''=0$–55 are indicated in order to show the range of the bound–bound transitions. Emission from $v'<10$ is completely bound–bound; the bound–free component increases for the higher v' levels. The spectra in fig. 5 are plots of Franck–Condon densities versus wavelength. They were calculated using standard computer programs, which we have implemented on IBM-PC compatible computers, for the following assumptions.

(1) The continuum levels in HgI(X) were calculated at 50 cm^{-1} intervals for transitions corresponding to $J'=J''=0$.

(2) The Franck–Condon factors for the bound–bound transitions were converted to Franck–Condon densities by dividing by 50 cm^{-1}, which is the sampling interval for the continuum levels.

(3) The calculated bound–bound and bound–free "lines" were convoluted with a Gaussian lineshape (fwhm = 50 cm^{-1}) in order to approximately account for the rotational envelope.

Fig. 6 shows the result from a weighted co-addition of the calculated spectra from $v'=0$–40:

$$I(\nu) = \left(\sum_{v'} I(v', \nu) \nu^3 P(v') \right) / \sum_{v'} P(v') \,. \qquad (4)$$

Since $N_2(A, v=0)$ provides up to 6.17 eV of energy and formation of HgI(B) requires 5.5 eV, the maximum energy available for vibrational excitation of HgI(B) was set as ≈ 0.67 eV or 5400 cm^{-1}. Therefore, the populations in levels with $G(v') > 5400$ cm^{-1} were set to zero. The steady-state distribution between $G(v')=0$ and 5400 cm^{-1} was taken as Boltzmann with a temperature of 8000 K. An equally good fit can be obtained using a linear surprisal distribution $P(v) = (1-f_V)^{3/2} \exp - \lambda_v f_V)$ with $\lambda_v = -1.0$, $f_V = G(v')/E_{max}$, $E_{max} = 5400$ cm^{-1}. The $\langle f_V(HgI) \rangle$ value for the distribution of fig. 6 is 0.44. There is good overall agreement between the synthesized spectra calculated for the $J=0$ potentials and the experimental HgI(B–X) spectrum.

We investigated further the sharp oscillatory struc-

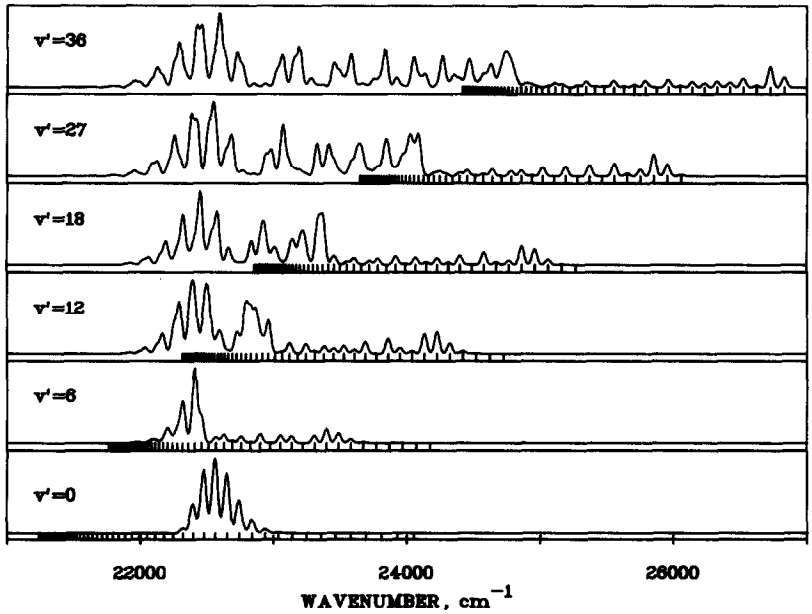

Fig. 5. Simulated spectra from selected HgI(B, v') levels based on Zhang et al.'s potentials and transition dipole function. The tick marks underneath each spectrum indicate the band origins for the ($v''=0$–55) progression. Transitions on the red side of the v''–55 band are bound–free. Continuum levels were sampled at 50 cm^{-1} intervals. All "lines" were convoluted with a Gaussian lineshape (fwhm = 50 cm^{-1}).

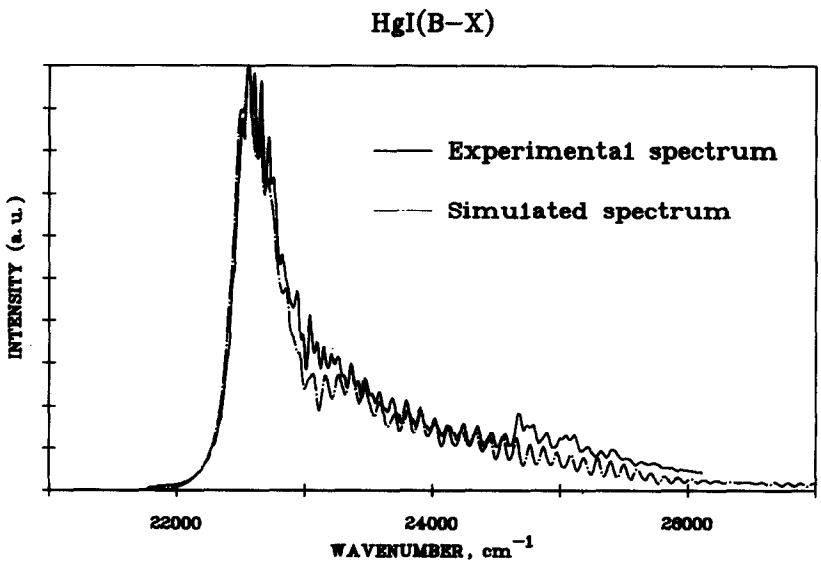

Fig. 6. Comparison of simulated HgI(B–X) spectra with a truncated 8000 K Boltzmann vibrational distribution ($J=0$, –·–) with the experimental spectrum (——). The main discrepancies are attributed to the scattered light from the N_2(C, $v'=0\rightarrow$B, $v''=4$) and N_2(C, $v'=0\rightarrow$B, $v'=3$) bands, which are near 23022 and 24634 cm^{-1}, respectively.

ture in the spectrum shown in fig. 6 by examining the effects of rotation. Strictly speaking, centering the rotational envelopes at the band origin ($J'=J''=0$) is hardly valid. For a thermal distribution of states, the peaks of the hypothetical Q-branch (ν_0') are shifted from the band origin (ν_0) by

$$\nu_0' - \nu_0 = 0.5kT(1 - B_{v'}/B_{v''}) - 0.25(B_{v'} - B_{v''}) . \quad (5)$$

Thus, the assumption is valid only for $v'-v''$ bands for which $B_{v'} \approx B_{v''}$, and the good agreement between the synthesized and experimental spectra in fig. 6 suggests that $B_{v'} \approx B_{v''}$ for the strongly favored $v'-v''$ bands. Fig. 7 compares calculated spectra from just $v'=0$ using three different treatments for the rotational states:

(a) $J'=J''=0$ (convoluted with a Gaussian lineshape, fwhm = 50 cm^{-1}).

(b) $J'=J''=84$ (convoluted with Gaussian lineshape, fwhm = 50 cm^{-1}).

(c) The true P and R branch lines with a 300 K distribution for N_J.

For the latter, the P and R branch lines were calculated (for each 0–v'' band) as:

$$\nu^{P(J)} = \nu_{v'v''} + F'(J) - F''(J+1) , \quad (6a)$$

$$\nu^{R(J)} = \nu_{v'v''} + F'(J) - F''(J-1) , \quad (6b)$$

$$I_{J' \to J''} = \frac{S_{J'}}{2J'+1} \frac{N_{J'}}{\Sigma N_{J'}} \nu^3 \langle 0|\mu|v''\rangle^2 , \quad (6c)$$

$$S_J^R = J' , \quad S_J^P = J'+1 , \quad (6d)$$

$$F(J) = B_v J(J+1) , \quad (6e)$$

$$B_v = \frac{h}{8\pi^2 \mu c} \langle v|1/R^2|v\rangle . \quad (6f)$$

The spectrum was calculated at 2 cm^{-1} intervals and the rotational lines were convoluted with a Gaussian lineshape (fwhm = 10 cm^{-1}). The comparison in fig. 7 shows that the $J=0$ calculation matches the true result better than the calculation with $J=84$, which is the mean rotational state at 300 K.

Fig. 8 shows an approximate deconvolution of the HgI(B–X) spectrum into is bound-bound and bound-free components. Trace (A) is the synthesized spectrum shown in fig. 6, trace (B) is the bound-free contribution, trace (C) is the high-reso-

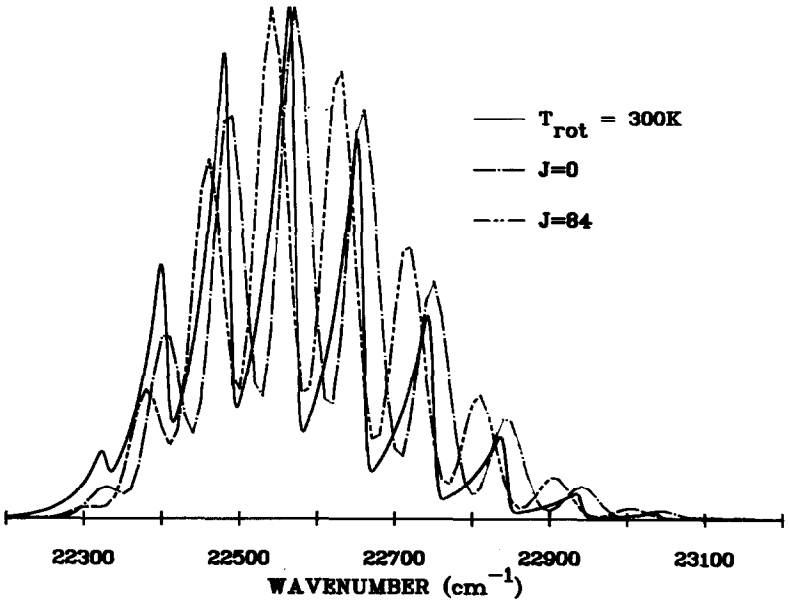

Fig. 7. Calculated bound–bound emission spectrum from HgI(B, $v'=0$) for three treatments of the rotational envelopes: (——) 300 K distribution of rotational states with Hönl–London factors for the line intensities for a $^2\Sigma^+$–$^2\Sigma^+$ transition with 2 cm^{-1} sampling and 10 cm^{-1} fwhm Gaussian line shape. (–·–) $J'=0$ with each band centered at the Q branch origin for 10 cm^{-1} sampling and 50 cm^{-1} fwhm Gaussian line shape, (– – – –) $J'=84$, which is the mean J for a 300 K distribution, with each band centered at the Q branch origin for 10 cm^{-1} sampling with 50 cm^{-1} fwhm line shape.

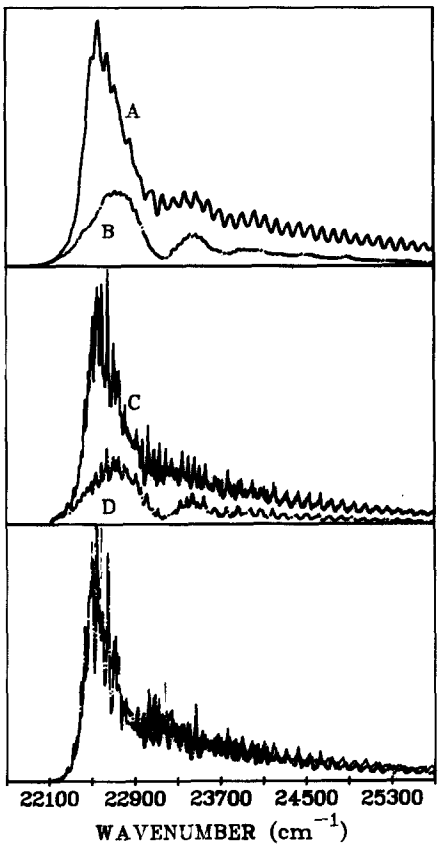

Fig. 8. Calculations illustrating the bound–bound and bound–free contributions to the HgI(B–X) spectrum for a 8000 K truncated Boltzmann distribution. (A) total simulated spectrum based upon $J=0$ potentials, (B) the bound–free contribution to (A), (C) the total experimental high-resolution spectrum from fig. 2, (D) the product of (C) and (B)/(A), i.e. the bound–free part of the experimental spectrum. The lower panel compares the rescaled experimental bound–bound spectra (C)–(D) and the calculated bound–bound spectrum for the full 300 K rotational distribution.

lution spectrum shown in fig. 2b, trace (D) is the bound–free component of the experimental spectrum which was obtained by multiplying trace (C) by the ratio of trace (B) to trace (A). Subtracting trace (D) from trace (C) yields the bound–bound component of the experimental spectrum, which is compared with the simulated bound–bound spectrum in the bottom panel using a 300 K thermal distribution of J' levels for $v'=0$–50, $v''=0$–47, $T_{vib}=8000$ K, $G_{max}(v')=5400$ cm^{-1}. The calculation was carried out in the same manner as described for $v'=0$ in eq. (6). The agreement between the experimental and simulated bound–bound spectrum is quite good, which establishes confidence in the potentials for HgI. Furthermore, the experimental HgI(B) rotational distribution from $N_2(A)+HgI_2$ appears to be nearly 300 K Boltzmann.

These calculations indicate that the sharp oscillatory structure in the HgI(B–X) spectrum also should have been observed from a HgI(B) distribution with a higher $\langle f_v \rangle$, such as that from Hg^*+I_2, if the rotational distribution was 300 K Boltzmann. The absence of structure in the spectrum from Hg^*+I_2 indicates a much broader HgI(B) rotational distribution.

4.3. Simulation of CdI(B–X) from $N_2(A)+CdI_2$

Spectroscopic information about the CdI(B and X) states is meager. The ω_e'' value has been assigned [30] as 179 cm^{-1} and D(CdI) has been estimated at 1.4 eV from the vibrational structures of the C–X, D–X, and E–X, transitions [35] and as 1.55 eV from thermodynamic data [11,24], see table 1. The rotational constants are unknown. Even less is known about the CdI(B) state. Greene and Eden estimated ω_e'' as 110 cm^{-1} based on the spacings of the oscillations in the emission spectrum for a relaxed CdI(B) vibrational distribution [35]. Our initial attempt to construct potential curves for the CdI(B and X) states was based on the following additional assumptions:

(1) The CdI(B) potential correlates with the ground state ions at the dissociation limit and should be well represented by a Rittner-type potential,

$$V(R)=T_e+D_e'+b\exp(-\beta R)-\frac{C_1}{R}-\frac{C_4}{R^4}. \quad (7a)$$

The dissociation limit, D_e', is above the CdI(X) dissociation limit, D_e'', by EA(I)+IP(Cd)$=-3.29+$ 8.99 eV. Since D_e'' is $\sim$1.55 eV, T_e+D_e' for CdI(B), relative to the CdI(X) minimum, is constrained to

$$T_e+D_e'=\mathrm{EA(I)}+\mathrm{IP(Cd)}+D_e''$$
$$=7.1\ \mathrm{eV}\ \ (\text{or } 57300\ \mathrm{cm^{-1}}). \quad (7b)$$

Since the polarizability of I^- is, at least, twice that of Hg^+ (estimated [26]) and Cd^+ should be less polarizable than Hg^+, the C_4 is determined by the polarizability of I^- and we used a value similar to HgI(B) (6×10^5 cm^{-1} Å^4). The value for C_1 is 1.1614×10^5

cm^{-1} Å. The parameters b and β were determined from the assumed ω_e'' (110 cm^{-1}) and R_e' (initially set at 3.3 Å, the same value as for HgI(B)):

$$\beta = \frac{k_e R_e^6 + 2C_1 R_e^3 + 20C_4}{C_1 R_e^4 + 4C_4 R_e}, \tag{8a}$$

$$b = \frac{C_3 R_e^3 + 4C_4}{R_e^5 \beta \exp(-\beta R)}. \tag{8b}$$

The force constant, k_e, was calculated from $k_e = 0.029711 \omega_e'^2 \mu$.

(2) By analogy with HgI(B–X), we first assumed that the maximum in the Franck–Condon density from CdI(B, $v'=0$) contributes to the intensity of the main band (but as will be seen below, this is not the case for CdI). Since the experimental spectrum peaks at ≈ 15160 cm^{-1}, initially $V_X(R=R_e')$ was set to be below $v'=0$ by this energy,

$$[G(v'=0) + T_e(B)] - V(R_e') = 15160 \text{ cm}^{-1}. \tag{9}$$

This was done by using a Morse function to represent CdI(X),

$$V(R) = D_e''\{1 - \exp[-\beta(R - R_e'')]\}^2, \tag{10}$$

with $D_e'' = 1.55$ eV (or 12500 cm^{-1}) and R_e'' set by using Greene and Eden's estimate of 2.4 eV for T_e(B). The Morse parameter β was calculated using $\beta = (k_e''/2D_e'')^{1/2}$ with $k_e'' = 0.029711(\omega_e'')^2\mu$ for $\omega_e'' = 179$ cm^{-1}.

(3) Since there was no information about the transition dipole, we assumed the same form as used for HgI(B–X) [26],

$$\mu(R) \alpha \exp[-2.2773(R-B)^n/E], \tag{11}$$

where B, n, and E are adjustable parameters. Initially, the maximum for the transition dipole, B, was set at $R_e' + 0.12$ Å with $n=2$ and $E=1.5$ for $R<B$, and $E=1.8$ for $R>B$. These choices are the same as those for HgI(B–X).

The calculation with the above parameters failed to yield a good simulation of the CdI(B–X) spectrum. However, by examination of the calculated spectra from individual v' levels and comparison with the oscillatory structure of the experimental spectrum, the potentials and transition dipole function were improved by trial and error. We will not present the sequence of the changes; rather the final results are summarized and the constants for the final B and X potentials, see fig. 9, defined with respect to the minimum of the CdI(X) potential are given in table 2. The main change, relative to the starting assumptions, was shifting R_e' relative to R_e''. We also did some calculations for D(CdI(X)) = 1.4 eV and a good fit to the spectrum could be obtained. However, we decided in favor of the thermochemical D(CdI) value and developed the X state potential accordingly. As shown in fig. 9, D(CdI) > D(HgI) leading to a much smaller R_e''(CdI). Therefore, the CdI(B–X) spectrum has a higher contribution of bound–bound transitions for the same $E_{v'}$ than does HgI(B–X).

The simulated and experimental spectra are compared in figs. 3 and 10. The vibrational distribution is a truncated 3000 K Boltzmann and the maximum energy available for vibrational excitation was taken as 6700 cm^{-1}. The mean fraction of vibrational energy is $\langle f_V(\text{CdI}) \rangle = 0.28$. The deconvolution of the CdI(B–X) spectrum into the bound–bound and bound–free contributions is shown in fig. 10. The most highly favored transitions from $v'=0$ are to the $v''=43$ and 44 levels, which are to the blue side of the

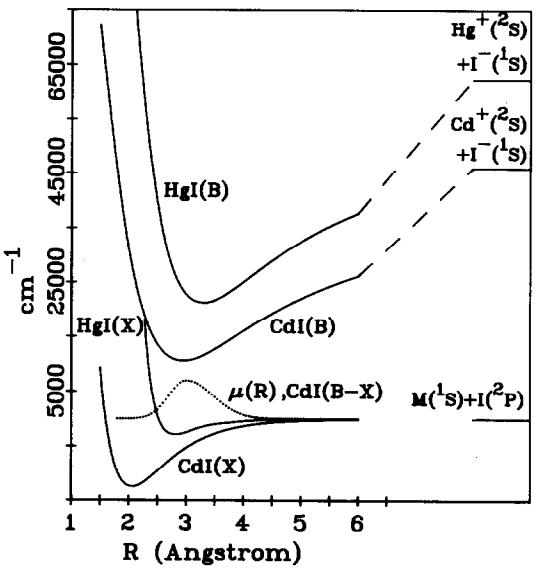

Fig. 9. The CdI(B and X) potentials and transition dipole function used for the simulation of the CdI(B–X) spectra shown in figs. 3 and 10. The HgI(B and X) potentials also are shown for reference. The CdI(B–X) transition dipole is shown as the dashed line.

Table 2
Constants for the CdI(X and B) potentials [a]

$V_B(R) = a + b\exp(-\beta R) - C_1/R - C_4/R^4$
$a = T_e + D'_e = 58483\ \text{cm}^{-1}$, $T_e = 23042\ \text{cm}^{-1}$, $D'_e = 35441\ \text{cm}^{-1}$, $b = 4.612384\times10^6\ \text{cm}^{-1}$, $\beta = 2.02171649\ \text{Å}^{-1}$,
$C_1 = 1.1614\times10^5\ \text{cm}^{-1}\ \text{Å}$, $C_4 = 6.0\times10^5\ \text{cm}^{-1}\ \text{Å}^4$, $R'_e = 2.944\ \text{Å}$, $\omega'_e = 110\ \text{cm}^{-1}$

$V_X(R) = D''_e\{1-\exp[-\beta(R-R''_e)]\}^2$
$R''_e = 2.058\ \text{Å}$, $D''_e = 12500\ \text{cm}^{-1}$, $\beta = 1.50896\ \text{Å}^{-1}$, $\omega''_e = 179\ \text{cm}^{-1}$

[a] The $V_B(R)$ potential should be used with caution for energy levels above 5000 cm^{-1}; the repulsive wall probably is too soft.

main band, as shown in plot (C) of fig. 3.

The oscillations in the CdI(B–X) spectrum are more pronounced than for HgI(B–X). These features are very sensitive to the choice for $R'_e - R''_e$, i.e. they correlate with the spacings of the v'' levels in the Franck–Condon region. By coincidence, the energy separations between the favored lower levels ($v'' = 40$–50) for transitions from the low v' levels are $\approx 110\ \text{cm}^{-1}$, which is similar to ω'_e thus giving rise to the pronounced structure in the spectrum. After the values of $R'_e - R''_e$ and T_e were established (from fitting the oscillations), R'_e was selected to satisfy the limit from eq. (7) within the uncertainty of the D''_e value.

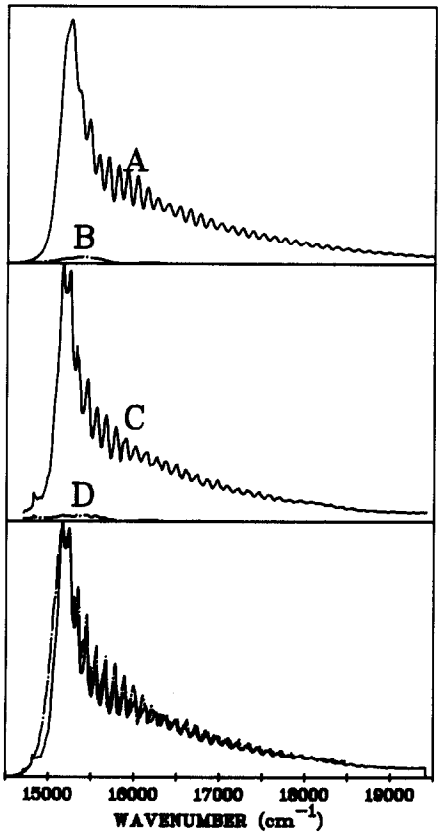

Fig. 10. Deconvolution of the experimental CdI(B–X) spectrum into bound–bound and bound–free contributions using the same procedure described in fig. 8 for HgI(B–X).

The initial assumptions about the transition dipole proved to be adequate, although a better fit was obtained using a sharper gradient for $R < B$ and E was reduced to 0.4 for $R < B$. The simulated spectrum was insensitive to values of E between 1 and 10 for $R < B$. Smaller E values at $R > B$ tended to enhance the depths of the oscillations. A more definitive determination of the transition dipole function would require either selective excitation of certain CdI(B, v') levels (see, for example, LeRoy's [36] simulation of the NaK(d–a) spectrum) or generation of CdI(B) with different $\langle E_V(\text{CdI(B)})\rangle$ from various reactions as was done for HgCl(B) by Zhang et al. [26].

4.4. An estimate for ω_e of ZnI(B)

The spectroscopic constants for ZnI(B) and ZnI(X) are less reliable than for CdI(B) and CdI(X). The current information about ZnI(X) is derived from the vibrational structure in the C–X, D–X, and E–X transitions. The ω''_e of ZnI(X) is assigned as 223.4 cm^{-1}, but estimates of the dissociation energy vary from 11000 to 19000 cm^{-1}. The only spectroscopic information available for ZnI(B) is the estimate by Greene and Eden [13] of $\omega''_e \approx 83\ \text{cm}^{-1}$, which was based on the separation of the bands in a relaxed ZnI(B–X) emission spectrum and upon analogy to CdI(B), then estimated to have $\omega'_e = 74\ \text{cm}^{-1}$, and $\omega'_e(\text{ZnCl(B)}) = 185\ \text{cm}^{-1}$. The rotational

constants for both states are unknown.

Simulating the ZnI(B–X) spectrum is not impossible, but many trial-and-error iterations would be required and the results, at best, would still be highly speculative until some of the constants are independently established. Thus, we will only present a new estimate for ω_e'(ZnI(B)), which should serve as an aid for future work on the ZnI(B–X) transition. Table 3 shows a comparison of reduced mass and ω_e values for several ionic metal halides. The force-constant comparisons were based on the relationship $\omega_e \propto (k/\mu)^{1/2}$.

The following two observations can be made.

(1) The MCl/MI force constant ratio, $(k_{Cl}/k_I)^{1/2}$, tends to be ≈ 1.25. If $(k_{ZnCl(B)}/k_{ZnI(B)})^{1/2}$ is 1.25 and if ω_e for ZnCl(B) is 185 cm^{-1}, then ω_e for ZnI(B) should be 108 cm^{-1}.

(2) The trends in properties of the lowest ionic state of the Zn, Cd and Hg iodides (the B state) should follow those of Ca, Sr, and Ba. The $(k_{CaI(X)}/k_{SrI(X)})^{1/2}$ and $(k_{CaI(X)}/k_{BaI(X)})^{1/2}$ ratios are both ≈ 1.05. Using this force constant relation with ω_e(CdI(B)) = 110 cm^{-1} gives ω_e(ZnI(B)) = 135 cm^{-1} and for ω_e(HgI(B)) = 110 cm^{-1} it gives ω_e(ZnI(B)) = 155 cm^{-1}.

The conflict between the prediction for ω_e(ZnI(B)) from (1) and (2) suggests that ω_e(ZnCl(B)) is too low.

According to observation (1), if the $(k_{HgCl(B)}/k_{HgI(B)})^{1/2}$ ratio is 1.25–1.15 and, if the currently accepted ω_e = (HgCl(B)) = 192 cm^{-1} is correct, ω_e(HgI(B)) should be 95–103 cm^{-1}. A lower ω_e(HgI(B)) would be consistent with the observation, lower part of table 3, that the row V and row VI metal halides tend to have a $(k_1/k_2)^{1/2}$ ratio of 1.02. With this ratio and ω_e = 110 cm^{-1} for CdI(B) ω_e(HgI(B)) should be ≈ 95 cm^{-1}. Therefore, a consistent set of ω_e values would appear to be 140, 110, and 98 cm^{-1} for ZnI(B), CdI(B), and HgI(B), respectively. However, the currently accepted ω_e = 110 cm^{-1} of HgI(B), which is based on standard spectroscopic analysis of the bound–bound HgI(B–X) spectrum [35] seems unlikely to be in error. These qualitative arguments must be regarded with caution. But, they do suggest that ω_e(ZnI(B)) is $\approx 140 \pm 10$ cm^{-1}.

We made an attempt to calculate the ZnI(B–X) spectrum by using Rittner and Morse potentials for the B and X states with $R_e' = 2.76$ Å and $R_e'' = 1.64$ Å

Table 3
Comparison of ω_e and force constants for some ionic states [a]

		ω_1/ω_2	$(\mu_2/\mu_1)^{1/2}$	$(k_1/k_2)^{1/2}$
CaCl(X)	CaI(X)	(1.54)	1.27	1.21
SrCl(X)	SrI(X)	1.74	1.38	1.26
BaCl(X)	BaI(X)	1.84	1.46	1.26
NaCl(X)	NaI(X)	1.42	1.18	1.20
KCl(X)	KI(X)	(1.51)	1.27	1.19
RbCl(X)	RbI(X)	(1.65)	1.43	1.15
CsCl(X)	CsI(X)	1.74	1.52	1.15
HgCl(B)	HgI(B) [b]	1.73	1.62	1.07
ZnCl(B)	ZnI(B) [c]	1.71 [c]		1.25 [c]
CaI(X)	SrI(X)	(1.37)	1.31	1.05
CaI(X)	BaI(X)	(1.56)	1.47	1.06
RbI(X)	CsI(X)	(1.16)	1.13	1.03
SrI(X)	BaI(X)	(1.14)	1.13	1.01
RbBr(X)	CsBr(X)	(1.13)	1.10	1.03
SrBr(X)	BaBr(X)	1.12	1.10	1.02
RbCl(X)	CsCl(X)	1.09	1.057	1.03
SrCl(X)	BaCl(X)	1.08	1.057	1.02

[a] Unless otherwise indicated, the constants were obtained from Rosen [30]. Numbers in parenthesis were based on constants from Huber and Herzberg [30].
[b] The HgCl(B) and HgI(B) ω_e values are from ref. [26].
[c] The ω_e of ZnI(B) as estimated in this work.

and the constants mentioned above. The choice for R_e'' followed from the expected T_e value and the choice for R_e' which was based upon analogy to CdI. This approach failed because the Rittner potential was not well behaved for vibrational levels above $v' = 10$. The attractive C_4/R^4 term appeared to be too large for the β and b values given by eq. (8).

5. Conclusions

The HgI(B–X) and CdI(B–X) emission spectra from the $N_2(A) + HgI_2$ and CdI_2 reactions have been simulated. The published spectroscopic constants for HgI(B, X) were found to be satisfactory, but improved potentials were required for CdI(B and X). Truncated Rittner and Morse parameterization for the B and X state potentials, respectively, proved to be adequate for simulating the CdI(B–X) spectrum. Independent assignment of some of the spectroscopic constants are needed before this approach can be successful for simulating the ZnI(B–X) spectra. The dissociative–excitation reactions of HgI_2 and CdI_2^* with $N_2(A)$ give high-temperature HgI(B) and CdI(B) vibrational distributions. The 300 K quenching rate constants for $N_2(A)$ by the metallic dihalide compounds are near to the gas kinetic limit. However, the branching fractions for MX(B) formation are generally small because of preferred formation of MX_2^* states that do not dissociate to MX(B).

Acknowledgement

We wish to thank Dr. F. Hartman, Mr. I. Hikmet and Mr. D. Jourdan for their assistance with spectral acquisition. G. Lo also thanks Université Joseph Fourier for a two month research appointment. The work at Kansas State University was supported by the United States Air Force Office of Scientific Research.

References

[1] J. Maya, IEEE J. Quantum Electron. 15 (1979) 579.
[2] J.A. McGarvey, N.-H. Cheung, A.C. Erlandson and T.A. Cool, J. Chem. Phys. 74 (1981) 5133.
[3] A.M. McCown, M.N. Ediger and J.G. Eden, Opt. Commun. 40 (1982) 190.
[4] M.N. Ediger, Q.W. McCown and J.G. Eden, Appl. Phys. Letters 40 (1982) 99.
[5] R.S.F. Chang and R. Burnham, Appl. Phys. Letters 36 (1980) 397.
[6] D.W. Fahey and L.D. Schearer, J. Chem. Phys. 72 (1980) 6318.
[7] T.D. Dreiling and D.W. Setser, Chem. Phys. Letters 78 (1980) 5439.
[8] T.D. Dreiling and D.W. Setser, J. Chem. Phys. 79 (1983) 5439.
[9] W.R. Wadt, J. Chem. Phys. 72 (1980) 2469.
[10] D. Husain, J.R. Wiesenfeld and R.N. Zare, J. Chem. Phys. 72 (1980) 2479.
[11] M. Kawasaki, S.J. Lee and R. Bersohn, J. Chem. Phys. 71 (1979) 1235.
[12] H. Hofman and S.R. Leone, J. Chem. Phys. 69 (1978) 3819.
[13] A.W. McCowan and J.G. Eden, Appl. Phys. Letters 39 (1981) 371.
[14] D.P. Green and J.G. Eden, Appl. Phys. Letters 43 (1983) 418; 42 (1983) 20.
[15] W.L. Nighan and R.T. Brown, J. Appl. Phys. 53 (1982) 7201.
[16] W.L. Nighan, Applied Atomic Collision Physics, Vol. 3. Gas Lasers, eds. F.W. McDaniel and W.L. Nighan (Academic Press, New York, 1982).
[17] P. Baltayan, J.C. Pebay-Peyroula and N. Sadeghi, J. Chem. Phys. 78 (1983) 2942; Chem. Phys. Letters 104 (1984) 168.
[18] P. Baltayan, J.C. Pebay-Peyroula and N. Sadeghi, J. Phys. B 18 (1985) 3615; 19 (1986) 2695.
[19] C.L. Bohler and L. Schearer, J. Chem. Phys. 89 (1988) 1950.
[20] V.I. Vedeneyev, L.V. Gurvich, V.N. Kondrasyev, V.A. Medvedev and Ye.L. Frankevich, Bond Energies, Ionization Potentials and Electron Affinities (Arnold, London, 1966).
[21] D.D. Wagman, W.H. Evans, V.B. Parker, R.H. Schumm, I. Halow, S.M. Bailey, K.L. Churney and R.L. Nuttall, J. Phys. Chem. Ref. Data 11 Suppl. 2 (1982).
[22] J.C. Queiroz, C. Airoldi and A.P. Chagas, J. Chem. Thermodynamics 18 (1986) 709.
[23] K. Wieland and R. Newburgh, Helv. Phys. Acta 25 (1952) 87; 22 (1949) 591.
[24] K. Wieland and A. Herczog, Helv. Chim. Acta 29 (1946) 1702.
[25] J.W. Simons, R.C. Oldenberg and S.L. Baughcum, J. Phys. Chem. 91 (1987) 3840.
[26] F.M. Zhang, D. Oba and D.W. Setser, J. Phys. Chem. 91 (1987) 1099.
[27] J.H. Kolts and D.W. Setser, Reactive Intermediates in the Gas Phase, Generation and Monitoring, ed. D.W. Setser (Academic Press, New York, 1979).
[28] D.S. Richards and D.W. Setser, J. Phys. Chem. 92 (1988) 3821.
[29] L.G. Piper, L.M. Cowles and W.T. Rawlins, J. Chem. Phys. 85 (1986) 3369.
[30] B. Rosen, Spectroscopic Data Relative to Diatomic Molecules (Pergamon Press, Oxford, 1970);
K.F. Huber and G. Herzberg, Constants of Diatomic Molecules (Van Nostrand–Reinhold, New York, 1979).
[31] D.Z. Cao and D.W. Setser, J. Phys. Chem. 92 (1985) 1169.

[32] M. Golde, Intern. J. Chem. Kinetics 20 (1988) 75.
[33] D. Lin, Y.C. Yu and D.W. Setser, J. Chem. Phys. 81 (1984) 5830.
[34] T.D. Dreiling, D.W. Setser and S. Ferrero, J. Chem. Soc. Faraday Trans. II 278 (1982) 1311.
[35] J. Tellinghuisen, P.C. Tellinghuisen, S.A. Davies, P. Berwanger and K.S. Visvanathan, Appl. Phys. Letters 41 (1982) 789.
[36] D.P. Green and J.G. Eden, J. Chem. Phys. 82 (1985) 702.
[37] R.J. LeRoy, W.J. Keogh and M.S. Child, J. Chem. Phys. 89 (1988) 4564.